REPORT DOCUMENTATION PAGE	*Form Approved* *OMB No. 0704-0188*

1. REPORT DATE *(DD-MM-YYYY)*	2. REPORT TYPE	3. DATES COVERED *(From - To)*
12-03-2012	Final Performance Report	May 1, 2008 to October 31, 2011

4. TITLE AND SUBTITLE

A Quantum Electronics Approach to Optical Negative Index Metamaterials (NIMs): Homogeneous NIMs in the Solid State

5a. CONTRACT NUMBER

5b. GRANT NUMBER

FA9550-08-1-0215

5c. PROGRAM ELEMENT NUMBER

6. AUTHOR(S)

Dr. Alkim Akyurtlu

5d. PROJECT NUMBER

5e. TASK NUMBER

5f. WORK UNIT NUMBER

7. PERFORMING ORGANIZATION NAME(S) AND ADDRESS(ES)

University of Massachusetts Lowell, Office of Research Administration
600 Suffolk Street, 2nd Floor South
Lowell, MA 01854

8. PERFORMING ORGANIZATION REPORT NUMBER

S51330000008312

9. SPONSORING/MONITORING AGENCY NAME(S) AND ADDRESS(ES)

USAF,AFRL DUNS 143574726, AF Office of Scientific Research
875 N. Randolph Street, Room 3112
Arlington, VA 22203

10. SPONSOR/MONITOR'S ACRONYM(S)

AFOSR/PKS

11. SPONSOR/MONITOR'S REPORT NUMBER(S)

AFRL-OSR-VA-TR-2012-0256

12. DISTRIBUTION/AVAILABILITY STATEMENT

DISTRIBUTION STATEMENT A. Approved for public release; distribution is unlimited.

13. SUPPLEMENTARY NOTES

14. ABSTRACT

Based on modern advanced methods of Quantum Optics, we discuss here the possibility of achieving the negative index of refraction in a semiconductor with donor-like impurities. This approach is genuine microscopic, and uses, instead of Maxwell equations (homogeneous NIM designs), the Quantum Mechanical methods. This design requires several specially prepared laser beams, one probe beam and several support beams, with specific intensities, frequencies and polarizations. These laser beams pump energy levels and create the desirable density matrix elements of an interest, which, in their turn, produce coherent permeability and permittivity responses at frequency of the probe laser beam.

15. SUBJECT TERMS

16. SECURITY CLASSIFICATION OF: a. REPORT	b. ABSTRACT	c. THIS PAGE	17. LIMITATION OF ABSTRACT	18. NUMBER OF PAGES	19a. NAME OF RESPONSIBLE PERSON
					Linda Concino
					19b. TELEPHONE NUMBER *(Include area code)*
					978-934-4750

Reset

FINAL REPORT

This final report details the theoretical and experimental work performed on the project titled, "A Quantum Electronics Approach to Optical Negative Index Metamaterials (NIMS): Homogeneous Negative Index Metamaterials based on Semiconductors from May 2008 - October 2011. Section A details the theoretical work and Section B details the experimental work. As a result of this work, the following papers have been accepted and presented at conferences:

1. Adil-Gerai Kussow and Alkim Akyurtlu, "Electromagnetically induced negative refractive index in doped semiconductors at optical frequencies", *Int. J. Mod. Phys. B*, 25, 347-364, March 2011
2. A. G. Kussow and A. Akyurtlu, "Homogeneous negative refractive index materials," *Journal of Nanophotonics*, 04(01), 043514, 2011
3. N. Wongkasem, C. Kamtongdee, A. Akyurtlu and K. A. Marx, "Artificial multiple Helices: polarization and EM properties, " *Journal of Optics*, **12**, 075102, June 2010
4. N. Wongkasem and A. Akyurtlu, "Light splitting effects in chiral metamaterials," *Journal of Optics*, **12**, 035101, January 2010
5. A. Akyurtlu and A-G. Kussow, "Low-Loss Negative Refractive Index Material Based on Doped Semiconductors: Quantum Optics Approach," 2010 IEEE International Symposium on Antennas and Propagation and URSI Radio Science Meeting, Toronto, Ontario Canada, July 11-17, 2010, accepted.
6. A. G. Kussow and A. Akyurtlu, "Negative refractive index in doped semiconductors," APS March Meeting, Portland, Oregon, March 2010.

A. THEORETICAL DEVELOPMENT OF NOVEL OPTICAL NIM

I. INTRODUCTION

Based on modern advanced methods of Quantum Optics, we discuss here the possibility of achieving the negative index of refraction in a semiconductor with donor-like impurities. This approach is genuine microscopic, and uses, instead of Maxwell equations (homogeneous NIM designs), the Quantum Mechanical methods. This design requires several specially prepared laser beams, one probe beam and several support beams, with specific intensities, frequencies and polarizations. These laser beams pump energy levels and create the desirable density matrix elements of an interest, which, in their turn, produce coherent permeability and permittivity responses at frequency of the probe laser beam. The quantum states of hydrogen-like donor atom embedded into solid state matrix and states of an electron in conduction band constitute a discrete-level atomic medium within the optical range. The coherent coupling of an electric dipole transition with a magnetic dipole transition leads to resonance-like permeability and permittivity responses, which, within some frequency band, ensures the negative refractive index. The implementation of this scheme is carried out in Sn-Zn-doped indium oxide, $In_{2-x}Sn_xO_3$:Zn (Zn-doped ITO), and the calculations show feasibility of the effect within a broad bandwidth with an extremely high figure of merit ($FOM = |\mathrm{Re}(n)/\mathrm{Im}(n)| \geq 10$) in the THz regime.

The main ideas behind the Quantum Optics approach which have developed recently will be described next. Several years ago, Oktel and Mustecaplioglu [1] suggested an elegant method to achieve the negative refractive index effect based on Quantum Optics. Despite the very different physics, their method is similar to electromagnetically-induced transparency formalism (EIT) [2]. Their model suggests the following arguments. The main difficulty of reaching the negative refractive index in the optical regime, in a homogeneous medium, is the frequency-dependent permeability function, $\mu(\omega)$, which in non-ferromagnetics, is close to 1 with no magnetic response. This behavior was explained by Landau [3], who showed that, in the optical regime, the projection of the magnetic moment, $\vec{\mu}$, of an individual spin, s, onto the high-frequency magnetic field, $\vec{H}(\omega)$, is almost zero due to the low frequency of the spin precession, $\omega_s = 2s\mu_B H/\hbar$ (μ_B is the Bohr magneton), compared to the frequency of the e.m. wave, ω. Note, that in *non-homogeneous* situation, this difficulty is avoided (at the expense of high scattering losses) due to the effective nature of $\mu(\omega)$ in such a way that the displacement currents or Mie resonances cause the considerable magnetic response which is effectively equivalent to $\mu \neq 1$.

We report here *solid-state-based* negative refractive index, homogeneous, and low-loss material. Obviously, as was mentioned in Ref. [1], since N in the solid state can be ~ 3-4 orders of magnitude larger than N in the gas phase, it would be extremely desirable to implement the solid state design. The solid state implementation, in principle, can allow for the desirable negative refractive index effect at THz (and higher) frequencies (the gas implementation [4-5, 6-9] so far provides the effect within MHz range, and not at THz range). Also, since the density of transitions is much higher in the solid state than in the gas phase, one might anticipate better parameters of the negative refractive index band in terms of the magnitude of the refractive index and the bandwidth.

This *solid-state-based* negative refractive index material is based on a n-type semiconductor doped simultaneously with a transition-metal (TM) with an atomic volume density, N, and p-type acceptor, with approximately the same density, N. The desirable negative refractive index effect is electromagnetically induced by the adjusted support e.m. fields (laser beams) to ensure the coherence of the dielectric and the magnetic responses. In accordance with band theory [10-12], the donor atom, or "defect", produces the discrete energy levels within the gap between the valence band and the conduction band (CB) (Fig. 1). The appropriate states of a donor can be treated as states of the hydrogen–like atom with re-normalized effective mass, m^*, of an electron and re-normalized effective charge, e^*, of an electron. Three first lowest-energy donor states are supplemented by the additional 4-th electronic state in the conduction band, to couple the donor states with the states of a crystal. The required non-zero magnetic moment between two hydrogen-like atom states with the same parities, but with mutually orthogonal radial wave functions is achieved by the specially oriented additional support beam which acts as a perturbation. Consequently, we explore the opportunity, by adjusting the parameters of the non-linear system (i.e. the density of the dopants, N, the intensities of e.m. fields of

the lasers, etc.) to achieve the desirable effect in the THz domain. All of the parameters, as we have mentioned above, are implemented for the specific example of tin-Zn doped indium oxide, $In_{2-x}Sn_xO_3$:Zn (Zn-doped ITO), to demonstrate the feasibility of the suggested design. In a detailed theoretical analysis, we have derived the quantum Louiville equations for the density matrix elements, ρ_{ij}, of the atomic states (indexes i and j denote atomic levels). Based on methods of Quantum Optics, these equations were solved and the solutions, for non-diagonal matrix elements with appropriate coherences are analyzed. Next, we have calculated the relevant dipole moments for the allowed dipole transitions between states with different parities. Afterwards, based on perturbation theory, we have calculated the induced non-diagonal magnetic moment element responsible for the transitions between states with similar parities. All of these density matrix elements, and the dipole and magnetic moments are utilized to calculate the dielectric response, $\varepsilon(\omega)$, the magnetic response, $\mu(\omega)$, and the refractive index, $n(\omega)$.

II. Atomic level system

In accordance with the band theory [10-12], in a n-type doped semiconductor, if the density of dopant atoms, N, is not too large, the states of the atoms are mutually independent and they correspond to well-isolated discrete energy levels within the band gap. The appropriate first 3 energy levels are shown in Fig. 1. The dopant atom, or zero-order defect, donates electrons of its outer electron shell into the conduction band (CB), and consequently, is effectively charged with some integer charge Z (Z =1, 2 or 3), depending on the type of the crystal and the type of a defect (dopant).

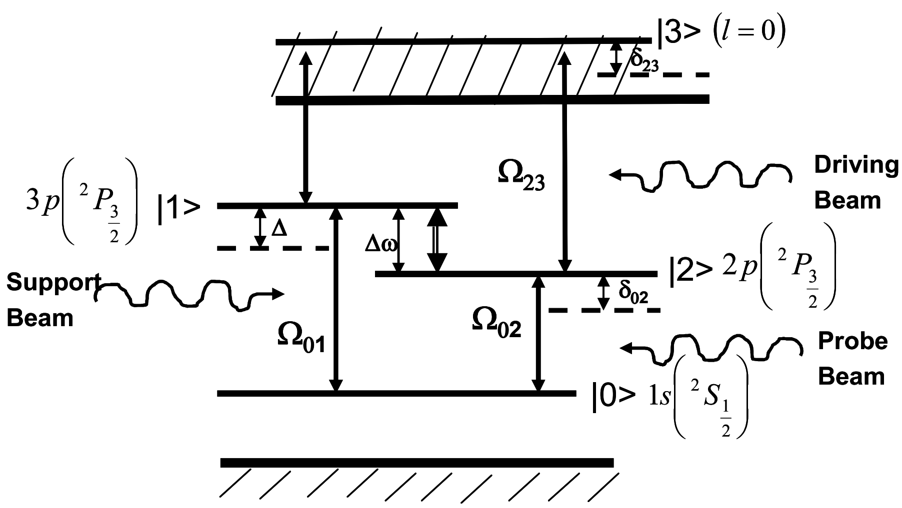

Fig. 1. System with discrete energy levels as described in text.

The long-range behavior of the defect potential $V(\vec{r})$ is described by the Coulomb-like potential of the electron with re-normalized effective mass, $m_0 \to m^*$, and re-normalized electron charge, $e \to e/\sqrt{\varepsilon_0}$, ($\varepsilon_0$ is a static dielectric constant) [10-11] . The appropriate Schrodinger equation provides the hydrogen-like wave functions, the Bohr radius,

$a_b = \hbar^2\varepsilon_0 / Zm^*e^2$, and the energy levels, $E_{nq} = -Z^2m^*e^4 / 2\hbar^2\varepsilon_0^2 n_q^2$, with $n_q = 1,2,3,....$ as main quantum numbers. We are interested in the first 3 lowest energy states ($n_q = 1,2,3$) which, in the text, are called 0-state (ground state, $n_q = 1$), 1-state (second excited state $n_q = 3$), and 2-state (first excited state $n_q = 2$). All energies, E_i, of these levels are below the bottom of the conduction band as shown in Fig. 1. The orbital quantum numbers, l_i, of these states, which define the parity, $P_i = (-1)^{l_i}$, are supposed to be: $l_0 = 0,\ l_1 = l_2 = 1$, to ensure the same parity of 1 and 2 states, which is different from the parity of the 0-state. The 4-th energy level (3-state) of our system is an electron energy level separated by the same distance from level 1 as level 2 (i.e. $E_3 - E_1 = E_1 - E_2$), and it has the same parity as the 0-state with $l_3 = 0$. The magnetic quantum numbers of all four states are the same (m = 0). The 3-state is inside the conduction band, and this state connects the isolated hydrogen-like atom states with the CB states of a solid-state matrix. The following electric dipole operators are non-zero: $<0|\vec{d}|1> \neq 0,\ <0|\vec{d}|2> \neq 0,\ <2|\vec{d}|3> \neq 0$, in accordance with the parities. The magnetic dipole operator $<1|\vec{\mu}|2> \neq 0$ between 1-state and 2-state can be non-zero, since parity rules, but it is actually zero in the undisturbed situation due to the orthogonality of the radial wave functions. Next, we introduce the four external electromagnetic fields which are to couple with these states. We assume that the probe e.m. field (beam b_2) provides a strong electromagnetic coupling for the electric dipolar transition $|0> \rightarrow |2>$ (the standard symbol |n> stands for the state n). This field is described by the amplitude, E_{02}, of the electric field with frequency, ω_{02}, detuning, δ_{02}, and the Rabi frequency, $\Omega_{02} = \vec{d}_{02}\vec{E}_{02} / \hbar$. The support e.m. field (beam b_1) is responsible for the weak electromagnetic coupling, $\Omega_{01} = \vec{d}_{01}\vec{E}_{01} / \hbar$, due to electric dipolar transition $|0> \rightarrow |1>$ with frequency, ω_{01}, detuning, Δ, and the Rabi frequency, $\Omega_{01} = \vec{d}_{01}\vec{E}_{01} / \hbar$ ($|\Omega_{01}| << |\Omega_{02}|$). The driving e.m. field (beam b_3) provides the weak electromagnetic coupling due to electric dipolar transition $|2> \rightarrow |3>$ between the atomic state and the solid-state matrix, with frequency, ω_{23}, detuning, δ_{23}, and the Rabi frequency, $\Omega_{23} = \vec{d}_{23}\vec{E}_{23} / \hbar$. All these e.m. fields are assumed to posses the same polarizations with collinear Poynting vectors, $\vec{S}_{01} \| \vec{S}_{02} \| \vec{S}_{23}$, and mutually parallel electric and magnetic fields ($\vec{E}_{01} \| \vec{E}_{02} \| \vec{E}_{23}, \vec{H}_{01} \| \vec{H}_{02} \| \vec{H}_{23}$).

III. Density Matrix

Such a system is described by a Hamiltonian in the form [5]:

$$\hat{H} = \hat{H}_0 + \hat{H}_i \tag{1}$$

where $\hat{H}_0$ is a field-free Hamiltonian and $\hat{H}_i$ is the interaction with the e.m. fields:

$$\hat{H}_0 = \sum_j E_j \,|\, j >< j \,| \tag{2}$$

$$< k|\hat{H}_i|l> = -\frac{1}{2}\hbar\Omega_{kl}e^{-i(\omega_k-\omega_l)t} \tag{3}$$

Here the Rabi frequencies associated with optical transitions are defined as $\Omega_{kl} = \vec{d}_{kl}\cdot\vec{E}/\hbar$ where $\vec{d}_{kl} = e < k|\vec{r}|l >$ is the electric dipole operator, e is the charge of the electron, and $\vec{E}$ is the amplitude of the relevant electric field. In the rotating-wave approximation, within the semiclassical theory of optical interactions [1, 5], the density matrix, $\hat{\rho}$, of the system evolves as required by the Louiville equations:

$$\frac{d\hat{\rho}}{dt} = -\frac{i}{\hbar}[\hat{H},\hat{\rho}] - \frac{1}{2}\{\Gamma,\hat{\rho}\} \tag{4}$$

$$\hat{\rho} = \sum_{k,l}\rho_{kl}e^{i(\omega_k-\omega_l)t}|k><l| \tag{5}$$

with diagonal elements of the relaxation matrix $< i|\Gamma|i> = \gamma_{ii}$ and off-diagonal elements defined as $< i|\Gamma|k> = (\gamma_{ii}+\gamma_{kk})/2$; the standard simbols [A, B] and {A,B} stand for the commutator, and symmetrized product of operators A and B, respectively. The detunings are defined by $\hbar\delta_{kl} = E_l - E_k - \hbar\omega_{kl}$ with ω_{kl} as the angular frequency of the appropriate e.m. field, and the detuning of the support field is called $\delta_{01} = \Delta$, so there are a total of three detunings: δ_{02}, δ_{23} and Δ.

Next, we need to obtain the solutions for ρ_{20}, ρ_{10}, ρ_{12}, ρ_{23}, and ρ_{31} of Eqs. (4), which affect the electric and the magnetic responses, and we will follow the EIT approximation [2] which is based on the usage of small parameters: $|\Omega_{01}/\Omega_{02}| << 1$; $|\Omega_{23}/\Omega_{01}| << 1$. The equations for ρ_{20}, ρ_{10}, ρ_{12} are split off from the rest of Eqs. (4) due to the strong interactions between 0, 1, and 2 levels. The system of three equations was solved, and the solutions for ρ_{10}, ρ_{20} and ρ_{12} are given by:

$$\rho_{20} = \frac{\Omega_{02}\exp[-i(\omega_{02}-\delta_{02})t]}{(\Delta-\delta_{32}-i\gamma'_{22})} \tag{6}$$

$$\rho_{10} = \frac{i\Omega_{01}[\gamma_{12}+i(\Delta-\delta_{02})]\exp[-i(\omega_{01}-\Delta)t]}{[(\gamma'_{11}+i\Delta)(\gamma'_{12}+i(\Delta-\delta_{02}))+|\Omega_{02}|^2]} \tag{7}$$

$$\rho_{12} = \frac{\Omega_{01}\Omega^*_{02}\exp[-i(\Delta\omega+\delta_{02}-\Delta)t]}{[(\gamma'_{11}+i\Delta)(\gamma'_{12}+i(\Delta-\delta_{02}))+|\Omega_{02}|^2]} \tag{8}$$

$$\boxed{\gamma'_{11} = (\gamma_{11}+\gamma_{00})/2;\ \gamma'_{22} = (\gamma_{22}+\gamma_{00})/2;\ \gamma'_{12} = (\gamma_{11}+\gamma_{22})/2,\ \omega_{02} = (E_2-E_0)/\hbar} \tag{9}$$

and $\Delta\omega = (E_1-E_2)/\hbar$ is the energy difference between level 1 and level 2. These solutions lead to the following non-diagonal element of the density matrix, ρ_{31}:

$$\rho_{31} = \frac{\Omega^{*}_{01}\Omega_{02}\Omega_{23}\exp[-i(\Delta\omega+\Delta-\delta_{02}-\delta_{23})t]}{(\Delta\omega-i\gamma_{13})[(\gamma'_{11}+i\Delta)(\gamma'_{12}+i(\Delta-\delta_{02}))+|\Omega_{02}|^2]} \tag{10}$$

Since we need to obtain an electric dipole and a magnetic dipole oscillating at the same frequency in order to modify the effective permittivity and permeability responses simultaneously, the coherence conditions require synchronization of frequency-dependent factors in Eqs. (6, 8, 10):

$$\omega_{02}-\delta_{02}=\Delta\omega+\delta_{02}-\Delta=\Delta\omega+\Delta-\delta_{02}-\delta_{23} \tag{11}$$

Equation (11) insists that the tunings are actually not independent:

$$\Delta=\Delta\omega-\omega_{02}+2\delta_{02} \tag{12}$$

$$\delta_{23}=2(\Delta-\delta_{02}) \tag{13}$$

Equations (12)-(13) express tunings Δ and δ_{23} as functions of the tuning of the probe beam, δ_{02}. Eqs. (12-13) correspond to the resonance situation when the e.m. field of the probe beam has frequency $\omega_{probe}=3Z^2m^*e^4/8\hbar^3\varepsilon_0^2-\delta_{02}$ and the e.m. field frequency for 0-1 transition is equal to the frequency for 2-3 transition, $\omega'_{01}=\omega'_{23}=2\omega_{probe}$, and it is twice larger than the ω_{probe}. Hence, all four of the effective energy levels are equidistant, and the support beams and the driving beams are degenerated since they have the same frequency. As a result, we will exclude the driving beam and leave only support beam with frequency $2\omega_{probe}$ with substitution $\Omega_{23}=\Omega_{01}$ into Eq. 10. Also, the probe beam causes two additional transitions, one is electric dipolar between levels 1 and 3, and another- magnetic dipolar transition between levels 2 and 1. The single tuning, δ_{02}, defines the frequency-dependence of both electric and magnetic responses.

IV. Permittivity and permeability functions

The classical electric dipole, $\vec{P}$, is calculated from the general expression [13] as:

$$\vec{P}=Tr\{\hat{\rho}\hat{d}\} \tag{14}$$

where $\hat{d}$ is the dipole operator. The amplitude of the electric dipole oscillating at frequency $\omega=\omega'_{02}$ of the probe e.m. field is defined by the 0-2 and 1-3 transitions:

$$\vec{P} = \vec{d}_{02}\rho_{20}+\vec{d}_{13}\rho_{31} \tag{15}$$

The effective electric polarizability second rank tensor, α_e, is defined by its Fourier transformation:

$$\vec{P}(\omega) = \alpha_e(\omega)\vec{E}(\omega) \tag{16}$$

where $\vec{E}$ is the electric field of the probe beam. Since we are interested in a single frequency ($\omega = \omega_{02}^{'}$), we will drop the ω dependence, and let $\alpha_e(\omega) = \alpha_e$. Since we will consider $\hat{d}$ parallel to the $\vec{E}$ direction, α_e is a scalar calculated from Eqs. (16), (6) and (10) as:

$$\alpha_e = \frac{d_{13}d_{02}\,|\,\Omega_{01}\,|^2}{\hbar(\Delta\omega - i\gamma_{13})[(\gamma_{11}^{'} + i\Delta)(\gamma_{12}^{'} + i(\Delta - \delta_{02})) + |\,\Omega_{02}\,|^2]} + \frac{d_{02}^2}{\hbar(\omega_{02} - \Delta\omega - i\gamma_{22}^{'})} \tag{17}$$

We should mention that the second term in the right part of Eq. (17) does not depend on the tuning, δ_{02}, and this term is much smaller than the first term. We also have included, into the expression for the effective permittivity $\varepsilon = 1 + 4\pi\alpha N$, $\vec{D} = \varepsilon\vec{E}$ (electric displacement), the Drude background permittivity, which is due to the free carriers (electrons) in the CB:

$$\varepsilon = \frac{4\pi N d_{13}d_{02}\,|\,\Omega_{01}\,|^2}{\hbar(\Delta\omega - i\gamma'_{13})[(\gamma_{11}^{'} + i\Delta)(\gamma_{12}^{'} + i(\Delta - \delta_{02})) + |\,\Omega_{02}\,|^2]} + \varepsilon_\infty\left(1 - \frac{\omega_p^2}{\omega^2 + i\gamma_p\omega}\right) \tag{18}$$

Here the Drude plasmon frequency, $\omega_p = \sqrt{\dfrac{4\pi n_c e^2}{\varepsilon_\infty m_{eff}}}$, depends on the concentration, n_c, of the free carriers in the CB, $\gamma_p \sim 0.1\omega_p$, and we use, in our calculations, the following concentration: $n_c \sim 10^{18}\,(1/cm^3)$.

The effective permeability, μ, is calculated from the classical magnetization, $\vec{M}$:

$$\vec{M} = Tr\{\hat{\rho}\hat{m}\} \tag{19}$$

where $\hat{m}$ is the magnetic moment operator. Again, we are interested in $\hat{m} = \vec{M}_{12}$ parallel to the magnetic field $\vec{H}$ of the probe beam, and ρ_{12} is the relevant ρ matrix element in Eq.(19). The effective μ, obtained analogous to the procedure described above, is given by:

$$\mu = 1 + \frac{\pi M_{12} N d_{01} d_{02}^{*} E_{01}}{\hbar^2[(\gamma_{11}^{'} + i\Delta)(\gamma_{12}^{'} + i(\Delta - \delta_{02})) + |\,\Omega_{02}\,|^2]} \tag{20}$$

Here, we assume a standard zero background magnetic response situation since no magnetic response to the field H within the optical domain is possible for non-ferromagnetic situation [3] .

V. Dipole and magnetic moments

To calculate the dipole moments, d_{01}, d_{02}, d_{13}, the wave functions of the atomic states are needed. These wave functions, are the products of the radial wave function $R_{nl}(r)$ and the angular wave function $Y_{lm}(\theta,\varphi)$ [13]:

$$\Psi_{nlm}(r,\theta,\varphi)=R_{nl}(r)Y_{lm}(\theta,\varphi) \tag{21}$$

The relevant angular wave functions are: $Y_{00}=1/\sqrt{4\pi}$ (0-state, 3-state), $Y_{10}(\theta,\varphi)\ =\ i\cos\theta\sqrt{3/4\pi}$ (1-state, 2-state), and the radial wave functions are given by:

$$R_{nl}(r)=-\{(\frac{2Z}{na})^3\frac{(n-l-1)!}{2n[(n+l)!]^3}\}^{1/2}\exp(-\frac{1}{2}\rho)L_{n+l}^{2l+1}(\rho) \tag{22}$$

$$L_{n+l}^{2l+1}(\rho)=\sum_{k=0}^{n-l-1}(-1)^{k+2l+1}\frac{[(n+l)!]^2\rho^k}{(n-l-1-k)!(2l+1+k)!k!} \tag{23}$$

with $a=a_b$ and $\rho=2Zr/na$. The calculation provides the explicit wave functions:

$$\Psi_{100}(r,\theta,\varphi)=\frac{1}{\sqrt{8\pi}}(\frac{2Z}{a})^{3/2}\exp(-\frac{Zr}{a})\quad \text{(0-state)} \tag{24}$$

$$\Psi_{210}(r,\theta,\varphi)\ =\ \frac{i}{2\sqrt{8\pi}}(\frac{Z}{a})^{3/2}(\frac{Zr}{a})\exp(-\frac{Zr}{2a})\cos\theta\quad \text{(2-state)} \tag{25}$$

$$\Psi_{310}(r,\theta,\varphi)=\frac{i}{12}\sqrt{\frac{3}{4\pi}}(\frac{2Z}{3a})^{3/2}(\frac{2Zr}{3a})(4-\frac{2Zr}{3a})\exp(-\frac{Zr}{3a})\cos\theta\quad \text{(1-state)} \tag{26}$$

The electric dipole operator, $\hat{d}=e\vec{r}$, has a $\hat{d}_z=er\cos\theta$ component in z-direction (spherical system of coordinates) which coincides with the direction of the electric field, $\vec{E}$, of the probe beam. Consequently, the dipole moments are given by the following integrals:

$$d_{02}=\int_0^{2\pi}\int_0^{\pi}\int_0^{\infty}\Psi^*{}_{100}(r,\theta,\varphi)er^3\cos\theta\,\Psi_{210}(r,\theta,\varphi)\sin\theta d\varphi d\theta dr \tag{27}$$

$$d_{01}=d^*{}_{13}=\int_0^{2\pi}\int_0^{\pi}\int_0^{\infty}\Psi^*{}_{100}(r,\theta,\varphi)er^3\cos\theta\,\Psi_{310}(r,\theta,\varphi)\sin\theta d\varphi d\theta dr \tag{28}$$

The dipole moments d_{01} and d_{02} calculated from Eqs. (21-28) are below:

$$d_{01}=d^*{}_{13}=\frac{81\sqrt{2}iea_b}{512Z} \tag{29}$$

$$d_{02} = \frac{8(2/3)^5 iea_b}{Z\sqrt{2}} \tag{30}$$

The magnetic dipole transitions, due to the parities, are allowed between states 1 and 2 if the magnetic dipole moment between these states is non-zero $M_{21} \neq 0$ (we assume the same spin wave functions $\chi_{1/2}$ for all states):

$$M_{21} = 2\mu_B \int_0^{2\pi}\int_0^{\pi}\int_0^{\infty} \Psi_{310}(r,\theta)\Psi_{210}^{*}(r,\theta)\sin\theta r^2 d\varphi d\theta dr(\chi_{1/2}\hat{s}\chi_{-1/2}) \tag{31}$$

with the spin factor $\chi_{1/2}\hat{s}\chi_{1/2} = 1/2$.
Since states 1 and 2 belong to the different shells, and the radial parts of wave functions, $\Psi_{210}(r,\theta)$ and $\Psi_{310}(r,\theta)$, are orthogonal to each other, the r-integral in the right part of Eq.(45), and, hence, the magnetic moment, M_{21}, both are equal to zero. To cope with this problem, we will consider the induced magnetic moment, M_{21}, due to the inhomogeneous electric field, $\vec{E}$, which causes the dipole moment-type perturbation $\hat{V}$:

$$\hat{V} = e\vec{r}\vec{E} \tag{32}$$

Here $\vec{r}\vec{E}$ is the scalar product of vectors. This field is oriented perpendicular to the other e.m. fields, in such a way that its electric and magnetic fields, $\vec{E}$, $\vec{H}$, and the Poynting vector, $\vec{S}$, are mutually perpendicular to $\vec{E}_{01}, \vec{H}_{01}$ and $\vec{S}_{01}$, appropriately. We assume that the relevant Fourier component of the electric field has an amplitude, E_0, and the fields $\vec{E} = \vec{E}_0 \exp(i\vec{k}\vec{r} + i\omega t)$, $\vec{H} = \vec{H}_0 \exp(i\vec{k}\vec{r} + i\omega t)$ are at a low frequency compared with the probe frequency (i.e. $\omega << \omega_{01}$). In the following text, it is convenient to rotate the initial system of coordinates (rotation angle $\theta' = \pi/2$) in such way that the new z-axis is perpendicular to the old z quantization axis, and the appropriate e.m. field of the probe and the perturbation e.m. field are perpendicular to each other: $\vec{E} \perp \vec{E}_p, \vec{H} \perp \vec{H}_p$. This transformation allows for the non-zero magnetic numbers $m = -1, -0, +1$ in the new system of coordinates, and the perturbation is expressed as:

$$\hat{V} = eE(r,\theta) r \sin\theta (e^{i\varphi} + e^{-i\varphi})/2 \tag{33}$$

Next, we will expand the long-wavelength perturbation into the series ($ka_b << 1$) with accuracy to two first terms:

$$\vec{E} \approx \vec{E}_0 (1 + i\vec{k}\vec{r} - \frac{1}{2}(\vec{k}\vec{r})^2) \tag{34}$$

We assume the complex wave vector, $k = k' + ik^{"}$, and the relevant part of the perturbation which contributes into the matrix element M_{21} is shown below:

$$\hat{V} = -eE_0(k'' - ik')r^2 \sin\theta \cos\theta (e^{i\varphi} + e^{-i\varphi})/2 \tag{35}$$

The perturbation above leads to the following matrix element, M_{12}, between state 1 and state 2 in accordance with the perturbation theory [13]:

$$M_{21} = \sum_{i,k} \frac{\mu_B (V_{ik} + V_{ki}) M^0{}_{kk}}{E_1 - E_2} \tag{36}$$

with three diagonal eigenvalues $M^0_{kk} = -1, 0, +1$ (magnetic quantum numbers) and indexes, i and k, which belong to 1-state and to 2-state, respectively. The calculation of V_{ik} from Eq. 36 with the angular wave function factors $Y_{1,0} = i\cos\theta\sqrt{3/4\pi}$, $Y_{1,\pm 1} = \mp i\sqrt{3/8\pi}\sin\theta e^{\pm i\varphi}$ yields the magnetic moment of an interest:

$$M_{21} \approx -\frac{0.62 e a_b^2 E_0 \mu_B (k'' - ik')}{Z^2 \hbar \Delta\omega} \tag{37}$$

VI. Negative refractive index band.

The complex refractive tuning-dependent index, $n = n(\delta_{02}) = \pm\sqrt{\varepsilon(\delta_{02})\mu(\delta_{02})}$, with the correct sign defined by the conditions [14-15] :

$$(|\varepsilon| - \mathrm{Re}(\varepsilon))(|\mu| - \mathrm{Re}(\mu)) > \mathrm{Im}(\varepsilon)\,\mathrm{Im}(\mu) \tag{38}$$

is expressed as a function of the probe frequency $\omega_{probe} = \omega_{02} - \delta_{02}$ (or tuning δ_{02}) with the following δ_{02}-dependence of both ε and μ:

$$\mu(\delta_{02}) = 1 + \frac{\pi M_{12} N d_{01} d_{02}^* E_{01}}{\hbar^2} F(\delta_{02}) \tag{39}$$

$$\varepsilon(\delta_{02}) = \frac{4\pi N d_{13} d_{02} |\Omega_{01}|^2}{\hbar(\Delta\omega - i\gamma'_{13})} F(\delta_{02}) + \varepsilon_\infty \left(1 - \frac{\omega_p^2}{(\omega_{02} - \delta_{02})^2 + i\gamma_p(\omega_{02} - \delta_{02})}\right) \tag{40}$$

The resonance-like function $F(\delta_{02})$ which enters Eqs. (39-40) is given by:

$$F(\delta_{02}) = \frac{1}{[(\gamma'_{11} + i(\Delta\omega - \omega_{02} + 2\delta_{02})(\gamma'_{21} + i(\Delta\omega - \omega_{02} + \delta_{02})) + |\Omega_{02}|^2]} \tag{41}$$

One can see from Eq. (41) that $F(\delta_{02})$ has two resonances at the frequencies $\delta_{02} = \delta_{res}^{\pm}$:

$$\delta_{res}^{\pm} = -\frac{3}{4}(\Delta\omega - \omega_{02}) \pm \sqrt{\frac{1}{16}(\Delta\omega - \omega_{02})^2 + \frac{1}{2}|\Omega_{02}|^2} \tag{42}$$

The behavior of the function, Re($F(x)$) with dimensionless parameter $x = \delta_{02} / \delta_{02}^{+} - 1$ is shown in Fig. 2.

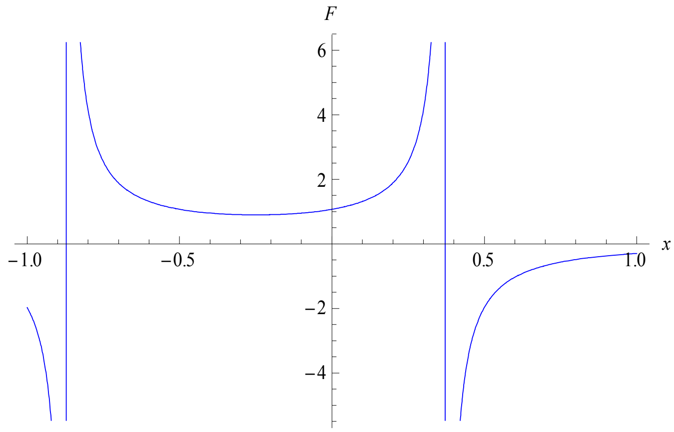

Fig. 2. The resonance function Re(F(x)) (Eq. (41)) in dimensionless coordinate of probe tuning

One can see that Re ($F(x)$) has two resonances. If $|\Omega_{02}| << |\Delta\omega - \omega_{02}|$, the right-wing solution $\delta_{res}^{+} = \omega_{02} - \Delta\omega = 11 Z^2 m^* e^4 / 36\hbar^3 \varepsilon_0^2$, and the other two tunings are: $\Delta = \delta_{res}^{+}$, $\delta_{32} = 0$. This resonance of interest exactly corresponds to the frequency $\omega_{probe}^{res} = \Delta\omega = 5Z^2 m^* e^4 / 72\hbar^3 \varepsilon_0^2$ of the probe e.m. field equal to the distance between levels 1 and 2. Expressions (38)-(42) were utilized to calculate both the real, Re(n), and imaginary , Im(n), parts of the refractive index, n, along with the figure of merit, FOM=|Re(n)/Im(n)|, as a function of the probe frequency ω_{probe} .

The specific material of choice is the transparent conducting tin-Zn-doped indium oxide, $In_{2-x}Sn_xO_3$:Zn (ITO doped Zn) [16-19], with the following relevant intrinsic parameters: Z=1, $\varepsilon_0 \approx 4.4$ [18] , $m^* \approx 0.3 m_e$ [19] (m_e is the mass of an electron), and a modest concentration of the carriers (electrons) in the CB $n_c \sim 10^{18}\,(1/cm^3)$, the level of doping for both In and Zn to be $N = 10^{21} cm^{-3}$. The level of losses $\gamma'_{11} \sim \gamma'_{12} \sim 10^8$ Hz was taken as lowest in gas phase [5], and then it was increased to a much higher level $\gamma'_{11} \sim \gamma'_{12} \sim 10^{10}$ Hz, to check the stability negative refractive index effect. The free parameter of the calculations was the probe beam laser intensity, I_p , which was changing in limits of experimentally established probe laser intensities $10^6\ W/cm^2 < I_p \le 10^8\ W/cm^2$ [20-21]. First, we calculated the frequency dependence of the complex permittivity $\varepsilon(\omega_{probe})$ and the permeability $\mu(\omega_{probe})$ which are shown in Figs. 3-4.

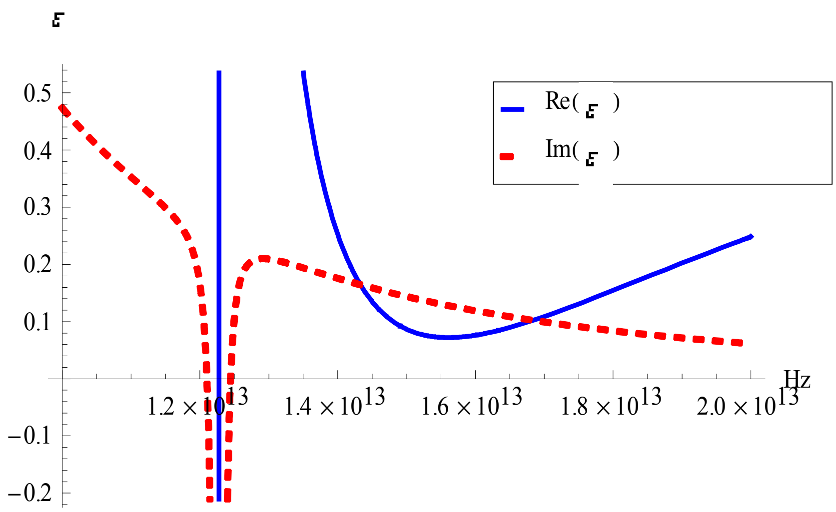

Fig. 3. The real (blue), $\mathrm{Re}[\varepsilon(\omega_{probe})]$, and the imaginary(red), $\mathrm{Im}[\varepsilon(\omega_{probe})]$, parts of the permittivity as a function of the probe frequency ω_{probe}. This is high loss situation, $\gamma'_{11} = \gamma'_{12} = 10^{10}\,Hz$, with probe laser intensity $I_p = 10^8 (W/cm^2)$, and doping concentration $N = 10^{21}\,cm^{-3}$.

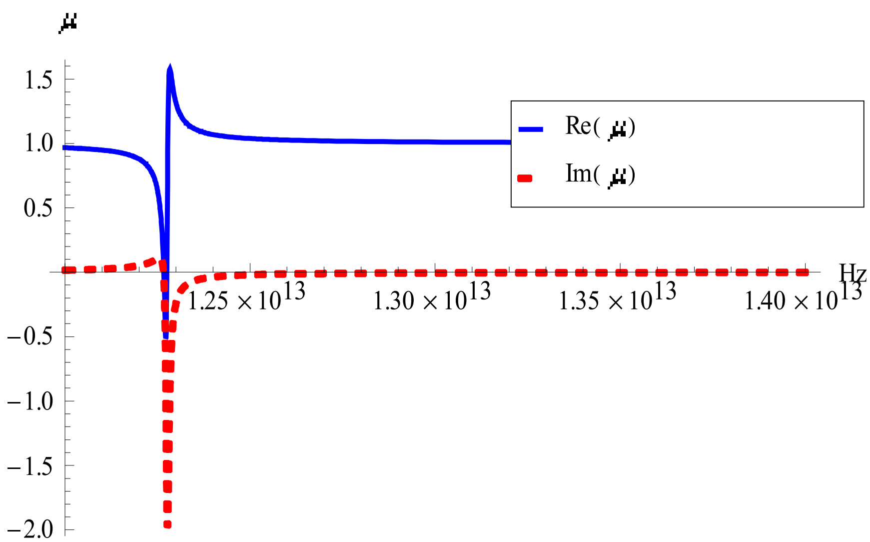

Fig. 4. The real(blue), $\mathrm{Re}[\mu(\omega_{probe})]$, and the imaginary(red), $\mathrm{Im}[\mu(\omega_{probe})]$, parts of the permeability as a function of the probe frequency ω_{probe}. This is high loss situation, $\gamma'_{11} = \gamma'_{12} = 10^{10}\,Hz$, with probe laser intensity $I_p = 10^8 (W/cm^2)$, and doping concentration $N = 10^{21}\,cm^{-3}$.

Fig. 5 demonstrates the frequency-dependent complex refractive index calculated for the probe laser intensities: $I_p = 10^8 (W/cm^2)$, which is within the modern limits of laser intensities. The negative refractive index band at ~ 12-13 THz is clearly seen with a well

pronounced real part of the index of refraction (Re(n)~ -1)), and a high FOM >10 (Fig. 6).

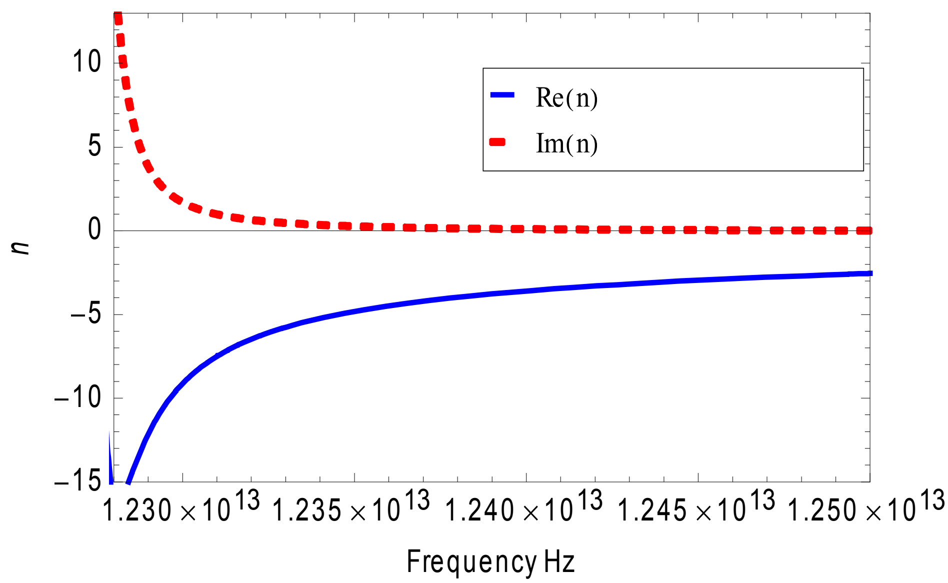

Fig. 5. The real (blue), Re($n(\omega)$) , and the imaginary (red), Im($n(\omega)$) , parts of the refractive index n as function of the probe frequency (Sn-Zn-doped indium oxide), all parameters are the same as in Figs. 3-4.

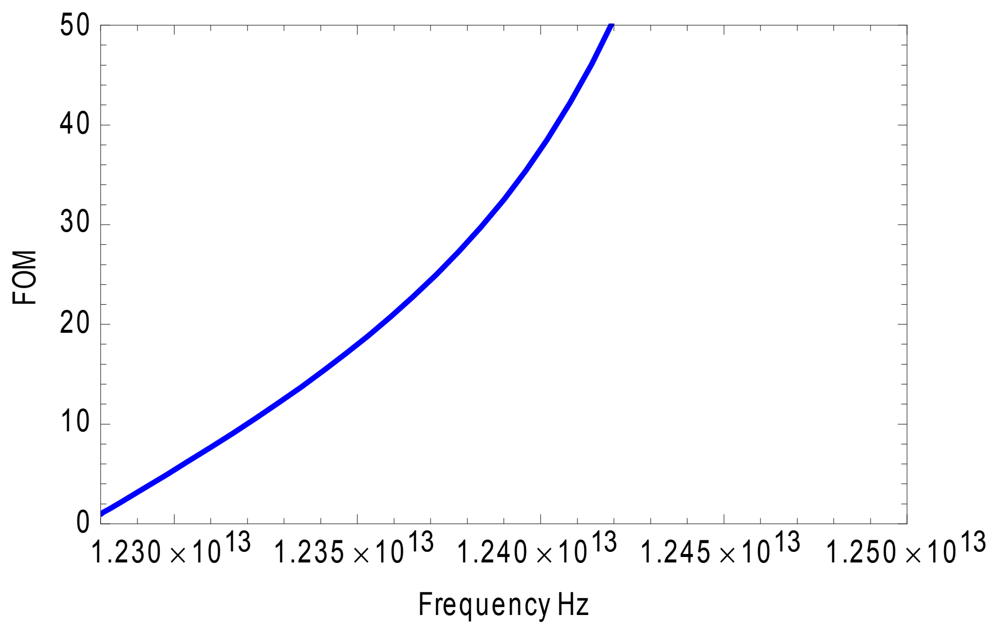

Fig. 6. Calculated figure of merit (FOM) as function of the frequency in Sn-Zn-doped indium oxide, all parameters are the same as in Figs. 3-4.

B. EXPERIMENTAL DEVELOPMENT

I. Introduction

The experimental approach to homogeneous NIMs included two different material systems: $(In_{1-x}Sn_x)_2O_3$ and Cr doped IO ($In_{2-x}Cr_xO_{3-\delta}$). Part 1 of this section will include the Sn doped IO system and will provide details of the fabrication methods, structural and optical characterization. Then it will describe an extraction methodology based on Nilsson's approach [22] on these films. Part 2 will present our most recent results on magnetic semiconductor (Cr doped IO) based homogeneous negative index materials. This section will provide details on the fabrication, structural, optical and magnetic characterization of $In_{2-x}Cr_xO_{3-\delta}$ films, and provide an alternative method for extracting the negative index of refraction of these materials based on reflection and transmission coefficients measured at multiple angles of incidence.

1. Sn doped IO material system

This section describes the structural and materials physics of the doped semiconductor $(In_{1-x}Sn_x)_2O_3$. The report is divided up into three sections 1) a description of the fabrication of the $(In_{1-x}Sn_{x/2}Zn_{x/2})_2O_3$ films and their structural, electronic and compositional characterization, 2) a report of the results of electromagnetic properties of the materials in the ultra-violet/visible spectral range and the mid-infra-red and 3) The computation of the real and complex parts of the refractive index. The real part of the refractive index can be pushed into the negative by pump and support laser fields, whereby electrical dipole transitions are magnetically coupled to produce a overlapping negative regions of dielectric permittivity and magnetic permeability. This produces the negative index effect which we look for with a probe laser which optically samples the region of the film, wherein the negative refractive index is produced.

The films are, at best, homogeneous polycrystalline smooth slabs of material with carrier densities and conductivities similar to those seen observed in n-doped semiconductors. We focus on a set of a series of In_2O_3 (IO) and $In_{2-x}Sn_xO_3$ (ITO) films, which serve as the basis set of samples for the growth and development of the $In_{2-x}(Sn,Zn)_xO_3$. The films are characterized by scanning electron beam (SEM) microscopy for homogeneity and smoothness, surface profiling for film thickness, energy dispersive X-ray spectroscopy (EDX) for sample composition, Hall measurements for electron concentration, optical transmittance by the spectrometry in the UV/Visible spectral region and the mid-infrared (mid-IR) spectral region using a Fourier transform infrared interferometer (FTIR).

The optical transmittance data can be fitted to a Drude plasmon model from which the high frequency permittivity can be extracted, along with the plasma wavelength, the bulk plasmon damping and, in principle, the effective mass. The transmittance and reflectance data are then used for computational extraction of the optical constants – n and k. All thin film samples were grown by sputtering on <100> p-Si substrates.

1.1 Crystal Structure and Film Fabrication

The quality of the sample material and the reproducibility of the observed optical properties are critically important to the success of this project. Over the last three months, a significant portion of time has been devoted to the development of the material sources. The doped (Sn, and Zn in this instance) In_2O_3 films in a DC and RF sputtering system. Several films of both IO and ITO (Sn doped In_2O_3) have been grown with varying Sn concentration and Ar gas pressure. The Ar gas pressure is used to sputter from the target and we have found that a pressure of 24 mT is conducive to the smooth and homogeneous films whose thickness lies in the range of several microns. This is ideal for the optical transmittance and EDX measurement considerations.

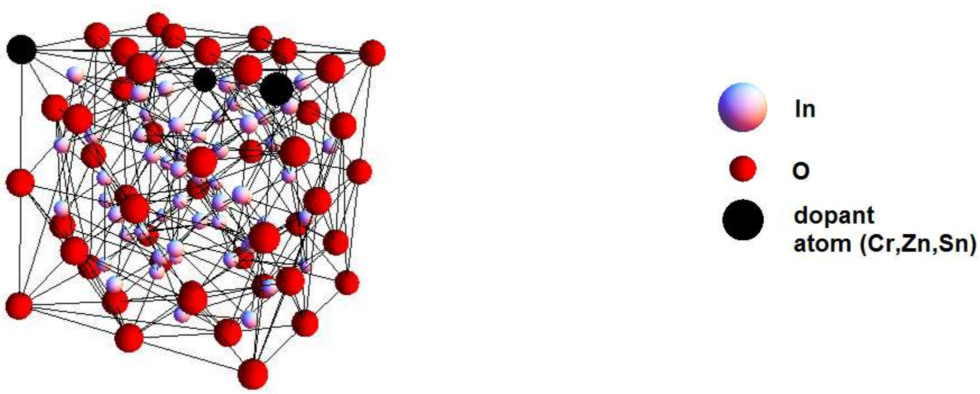

Fig. 2 (a)The cubic bixbyite structure of (II,VI) randomly doped In_2O_3

The thicknesses are measured by surface profiling and, more accurately, by measuring the separation in adjacent Fabry-Perot (FB) interference fringes in the transmittance data. These FB oscillations can be observed in the mid-IR range for films of several microns in thickness. SEM imagining reveals the surface morphology and smoothness of the films.

The Sn and Zn dopant atoms will be independently controlled in terms of sputtering rates and hence the deposition of these atoms into the insulating In_2O_3 matrix is done in order to controllably balance the density of these two atomic species.

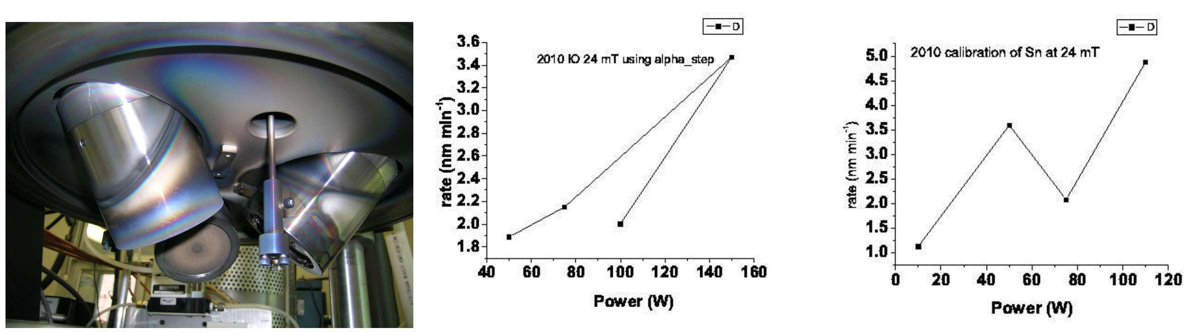

Fig. 2 Sputtering chamber photograph showing the sputtering guns. The calibration curve enables the control of the composition of the film with Sn/Zn gun power. The plots Show the growth rate calibration for deposition rate Vs. power.

1.2 Electrical and Compositional Characteristics

The optical scattering and losses are critically dependent upon the carrier density. This we measure using a Hall setup, from which the Hall constant and mobility are derived. The typical Hall carrier concentrations that are measured in the intrinsic In_2O_3 are in the range of $1x10^{18} – 5x10^{19} cm^{-3}$. This concentration is pushed upwards by the addition of Sn atoms into the material, as shown in Table 1.

In order to gain an understanding of the composition of the IO and ITO films, we subject our films to EDX analysis with a field emission SEM. This beam penetrates a distance of about 1 micron into the sample. The accumulated statistics on collected keV dispersive energies, reveal the Sn (Z=49) peak, which have had to have been separated from the In (Z=50) peak. From these atomic percentages, we calculated the mole ratios, x, and the resulting carrier concentrations as measured by the Hall measurements. We find that, in general, the carrier density is determined completely by the Sn mole ratio (x) and the oxygen mole ratio 3-δ in the formula $In_{2-x}Sn_xO_{3+\delta}$.

Table 1. Summary of the EDX material composition analysis of the DC/RF co-sputtered ITO films. The carrier concentration is measured by the Hall effect.

In2-xSnxO3							
sample	In at.%	Sn at. %	x	Δx	density (cm^-3)	O at. %	thickness (μm)
sp10-016	26.43	0.23	0.01725431	0.014381161	9.61E+19	45.86	1.5
sp10-017	26.11	1.36	0.09901711	0.014090541	3.69E+18	43.95	1.17
sp10-018	61.05	2.53	0.07958478	0.006066175	5.84E+20	20.26	1.06
sp10-019	26.46	0.97	0.07072548	0.014041874	2.44E+21	45.2	0.619
sp10-020	60.89	3.04	0.09510402	0.006049774	6.19E+20	19.78	1
sp10-021	42.37	7.77	0.30993219	0.008530097	9.80E+20	16.89	0.316
sp10-022	67.79	2.67	0.07578768	0.005470576	3.41E+20	22.95	1.82
sp10-023	60.54	0.9	0.02929688	0.006243564	1.20E+21	21.49	1.03

1.3. Optical characterization in the UV/visible

In order to understand the optical characteristics of the IO and ITO films in the visible region of the electromagnetic spectrum, we performed transmittance measurements on the samples using a broadband halogen and deuterium lamp and an Avantes 3000 visible/UV spectrometer. We were able to resolve clear Fabry-Perot oscillations in the IO films, indicating their smooth and optically homogeneous quality. The UV/Visible transmittance measurements also revealed strong and pronounced inter-band absorption at around 350nm (see Figure 3 (a)), which is corresponds to a band gap of 3.1-3.55 eV (Figure 3 (b)) and the absorption occurs between the between O (2p) and In (5s) states in the material.

(a)

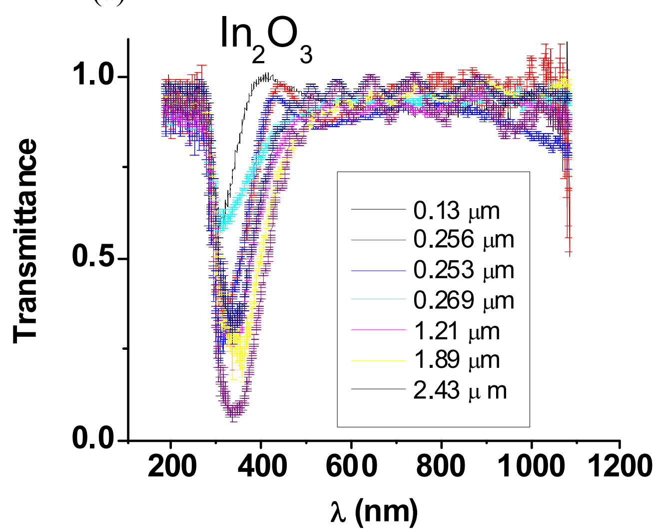

(b)

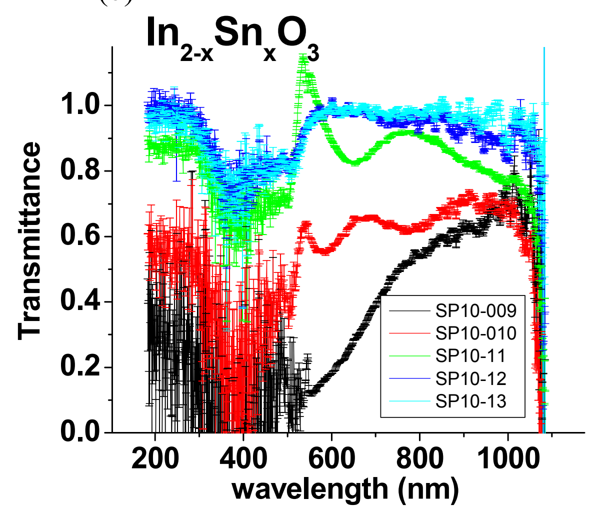

(c)

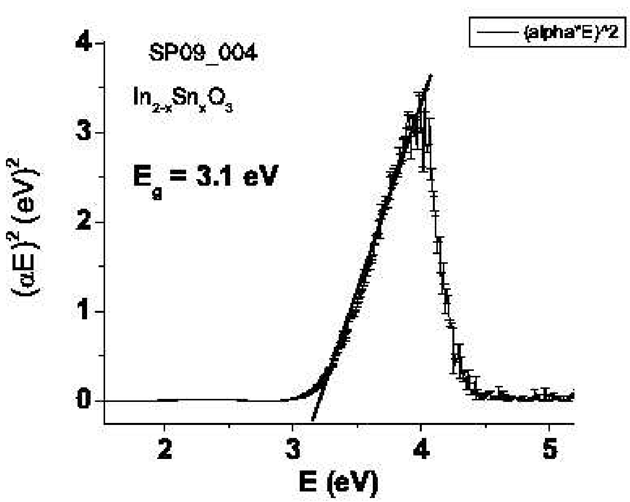

Fig. 3 (a) Transmittance curves of the indium oxide films showing Fabry-Perot oscillations from which the thicknesses were extracted. The dips at 350nm indicate interband absorption. (b) Optical transmittance curves for the ITO films – showing the suppression of the interband absorption due to scattering losses. (c) the band gap estimate linear fit for a typical sputtered IO film .

Figure 3(b) shows the plots of the transmittance for the ITO films. These plots demonstrate that these films are more lossy, due to the inclusion of the Sn substitutions.
The interband transitions are screened out, yet the Fabry-Perot oscillations are still present, indicating that the films are smooth on the length scales of the probing wavelength. These films of ITO are now ready for the doping of the Zn atoms. The Zn

atoms, unlike the Sn atoms, which donate one electron to the conduction band, are acceptors and give two holes to the conduction band. The Zinc atoms are to be used to reduce the total carrier concentration while maintaining a Sn doping mole ratio of about x=0.05.

1.4 Optical characterization in the mid-IR

We performed transmission measurements on the IO and ITO films using broadband THz radiation with a Brueker Optics Vertex 70 FTIR incorporating a room temperature CsI DLATGS detector, whose sensitivity falls in the wavelength range 2.5 μm to 30 μm. The substrate material p-Si offers a 50 % transmittance in this range. This substrate is used to characterize our background signal. \ The optical constants and the parameters of the electric permittivity function, are found from the extraction procedure as described by P. O. Nilsson using the formalisms developed by Mayer and Heavens. The extraction of the Drude parameters are done by fitting the transmittance curves to a Drude model. This latter procedure is absolutely necessary to establish whether we have negative permittivity in the mid-IR region.

1.5 Drude plasmon fitting

In order to extract the theoretically intractable parameter $\in_\infty$, together with the bulk plasma wavelength and the plasmonic losses, we fit the mid-IR transmittance data to a model of the permittivity function. This is done by writing the Drude model for the dielectric permittivity, as follows:

$$\varepsilon(\lambda) = \varepsilon_\infty \left(1 - \frac{\frac{\lambda^2}{\lambda_p^2}}{\left(1 + i\Gamma \frac{\lambda}{\lambda_p} \right)} \right)$$

Where $\in_\infty$ is the high frequency dielectric permittivity, λp is the plasma wavelength and Γ parameterize the losses. The transmittance is then calculated in terms of the Fresnel formulae and a fit with the mid-IR transmittance data is done. A typical fit is depicted in Figure 4, while the table of fitted parameters are given in Table 2.

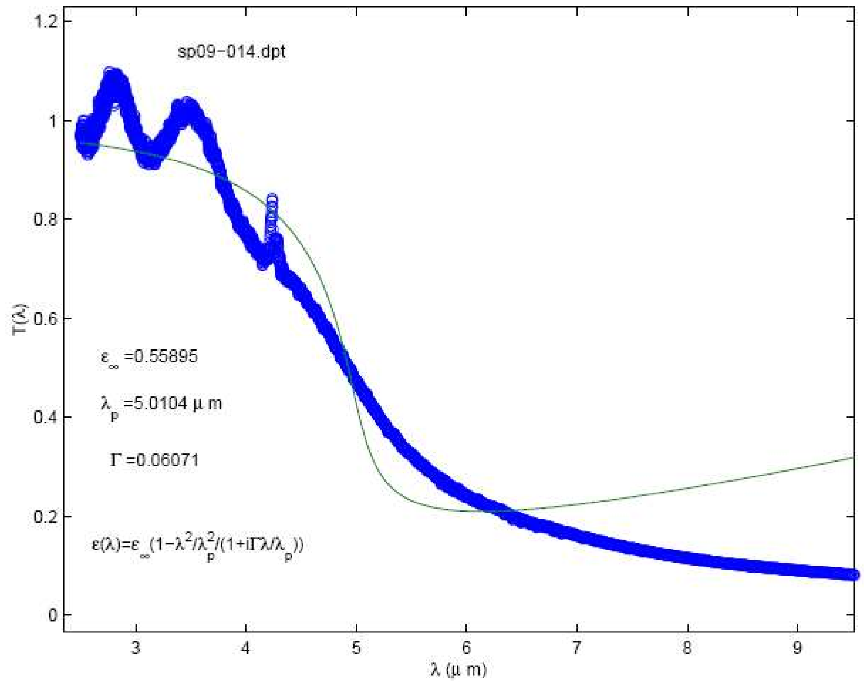

Fig. 4 A typical fit of the mid-IR transmittance curve for an IO sample in order to extract the 3 Drude parameters of the Drude model. The plasmon losses are underestimated here And the long wavelength fit is divergent from the data, as are the data in the Fabry-Perot interference region.

Table 2. Drude model fits to the transmittance data of a series of indium oxide films.

Sample#	εinf	λP(um)	Γ	Fit convergence (chi sq.)
09-012	0.031413	9.7854	0.53037	0.174118
sp09-10	1.294	12.6477	0.014763	0.03
sp09-13	0.051615	13.1977	0.46964	0.0342691
sp09-14	0.55895	5.0104	0.06071	15.4424
sp10-26	0.051433	14.7177	0.5387	0.0664292

1.6 Numerical extraction of the optical constants

In order to accurately extract the optical constants of the films (the real and imaginary parts of the refractive index), we model the optical transmittance and reflectance using the methods described in Refs 22-24. The idealized film/substrate/air system as considered in the paper can be represented in the following way:

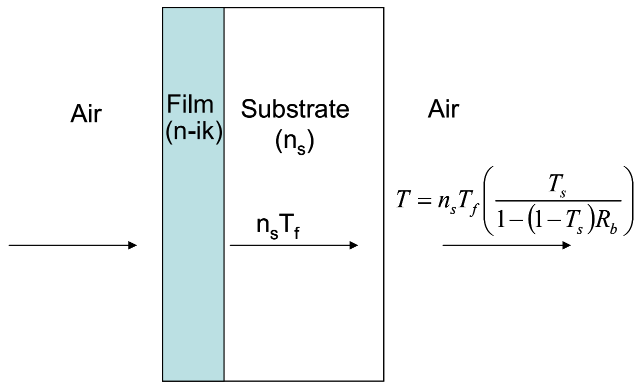

The equations which relate the film properties and the measured transmittance and reflectance are strongly non-linear and implicitly specified as follows:

F(T,n,k) = 0 and G(R,n,k) = 0

The right hand side of these equations is taken to be squared and this is the functional to be minimized for the extraction of the optical constants of the film in question.

The Nilsson extraction procedure is very powerful for the ITZO optically pumped negative index experiment because all of the optical constants of a film can be extracted from a single shot, low noise transmittance experiment over a finite spectral range. The phase can also be estimated, eliminating the need for the use of the Kramers-Kronig relations, altogether. This method of the determination of the optical constants for the film is crucial as the probe laser will be collinear and coincident with the pump and support beams, and will be critical for accurately determining n and k under the requisite Photon pumping conditions.

2. Cr doped IO material system

In this section we will discuss in detail the homogeneous NIMs based on magnetic semiconductor $In_{2-x}Cr_xO_3$. We have shown that a strongly pronounced negative refractive index effect at ~ 27.8 μm. This effect was theoretically predicted earlier, and it is based on coexistence of the spin wave (magnon) mode with the plasmonic mode, with simultaneous negative permittivity and permeability responses. The thin films of $In_{2-x}Cr_xO_3$ are fabricated, with low stoichiometric oxygen deficiency, which is required for ferromagnetic behavior. The magnetic measurements clearly reveal the ferromagnetism with high saturation magnetization. The complex frequency-dependent refractive index is extracted from combined transmittance and reflectance data.

Theoretical studies of Cr doped IO, [25] predict that such principally homogeneous materials (monocrystals or polycrystals) belong to class of *magnetic semiconductors* with ferromagnetic behavior, and detailed calculations of the expected negative refractive index were done for the transparent conducting Cr-doped indium oxide [26]. The calculations show that this ferromagnetic system, in its polycrystalline form, should possess the fully *isotropic,* low-loss negative refraction index $n < 0$ at ~ 10.48 THz. The negative refraction index was owing to overlapping the negative permittivity function $\varepsilon(\omega) < 0$, due to the plasmons (resonance frequency ω_p), with the negative permeability function $\mu(\omega) < 0$ due to the spin waves. In support of the idea of homogeneous materials with desirable effect, it was demonstrated experimentally [27], that ferromagnetic metal mangenite, $La_{2/3}Ca_{1/3}MnO_3$, reveals negative refractive index at ~ 150 GHz, based on analogous plasmon-magnon excitation mechanism.

2.1 Fabrication of Cr doped IO material system

Fabrication of *ferromagnetic* $In_{2-x}Cr_xO_{3-\delta}$ films is a considerable challenge itself since the ferromagnetic behavior of $In_{2-x}Cr_xO_{3-\delta}$ critically depends on the stoichiometric oxygen deficiency concentration, or parameter, δ which should be within the difficult-to-reach narrow range: $1.6\times10^{-4} \le \delta \le 10^{-2}$ [28]. Since every oxygen deficiency provides 2 electrons into the conduction band, the δ controls the electron density, n_e, in conduction band. As the ferromagnetic ordering in this material is electron-mediated, and heavily depends on n_e., the required δ within the aforementioned narrow range is crucial for indirect spin coupling, which causes the ferromagnetism [28]. Also, additional details of the fabrication process dramatically affect the magnetic behavior of the Cr-doped IO, and for this reason, the ferromagnetism becomes elusive or difficult to reach. Moreover, several groups, for this very reason, even deny the very existence of the ferromagnetic properties [29-30] or suggesting the presence of secondary phase as the origin of ferromagnetism [31-32].

To cope with this difficulty, we have used an effective post annealing process for precise control of structural parameter δ. The material growth technique used for depositing the thin films was based on the DC/RF magnetron sputtering technique. The sputtered samples are deposited in a chamber whose base pressure was maintained at around 2×10^{-7} Torr and the films were deposited on p-Si (100), whose resistivity was on the

order of 0.1 Ω cm. In terms of substrate temperature, the grown samples are synthesized at room temperature.

The sputtered samples are grown using two targets - a d.c. magnetron sputtering gun for the Cr and an r.f. magnetron gun for the In_2 O_3 Cr/ In_2 O_3 targets (K.J. Lesker, both at purity of 99.99%). The sputtering is performed in an Ar atmosphere of around 24 mT, while the oxygen concentration can be enhanced by the inclusion of a small partial pressure of oxygen at around 0.3×10^{-3} mT. The oxygenation comes from a rf driven O_2 plasma source and is controlled by a needle-valve and mass flow controller 5.8 sccm. In this way, we have grown Cr doped indium oxide with the general formula of $In_{2-x}Cr_xO_{3-\delta}$ (ICO), where x is the Cr mole fraction and δ represents the deviation from stoichiometric oxygen content. These samples were post annealed at 250^0 C in air. Even a tiny change in the wt% of the oxygen results in a significant change in the oxygen deficiency, δ.

The stoichiometric composition required for ferromagnetism is within the following range: 38.80±0.506 wt % In, 60.00±0.108 wt% O with 1.20±0.398 wt% Cr. In order to obtain this composition, the fabricated samples are post annealed at 250 ^{0}C. It is known that annealing in vacuum results in the formation of oxygen vacancies [33-34]. On the contrary, annealing of CIO in air causes oxygen to re- diffuse into the film and eradicates the oxygen vacancies. EDS results are presented in Table 1 below. As follows from this table, by changing the time of annealing (60 sec), we were able to reach the aforementioned range [28] for δ.

TABLE I. The effect of post annealing time on the composition of the sputtered Cr-doped InO

Annealing	%O	%Cr	%In	X	δ
As-deposited	75.91	1.23	22.85	0.102	-3.3048
250^0C in 45 sec.	59.40	0.75	39.85	0.037	0.0739
250^0C in 60 sec.	59.93	0.73	39.34	0.036	0.0087
250^0C in 50 sec.	64.14	1.01	34.86	0.056	-0.5762
250^0C in 55 sec.	62.89	1.18	35.93	0.064	-0.3894

2.2 Characterization of Cr doped IO material system

The ordinary Hall Effect with a Van der Pauw contact geometry was used to determine the conduction carrier concentration, n_e. The structural study of the fabricated samples was done by energy dispersive spectroscopy, EDS, and the film thickness was measured by the AlphaStep profilometer instrument.

The magnetic measurements of the successful samples are performed by SQUID at 10 K and at room temperature, in hope to see expected ferromagnetic behavior. The magnetic field is applied in the sample plane. Fig. 1 shows the results of the magnetization versus applied magnetic field (M-H) curve measured at 10 K for the 0.35 µm thick of Cr:InO

annealed thin films with carrier density n_e= 0.529 x10^{19}. As follows from this result, our successful samples are indeed ferromagnetic, with high saturation magnetization up to 0.6 μ_B/Cr-atoms. The measurements of the ferromagnetic thin samples with thickness 0.1 μm provided even higher saturation magnetization up to 0.8 μ_B/Cr-atoms. Since this saturation magnetization is only ~ 25% larger than magnetization 0.6 μ_B/Cr-atoms for thick samples, we can conclude that magnetization is mostly bulk effect and surface enhances ferromagnetism only to a small extent.

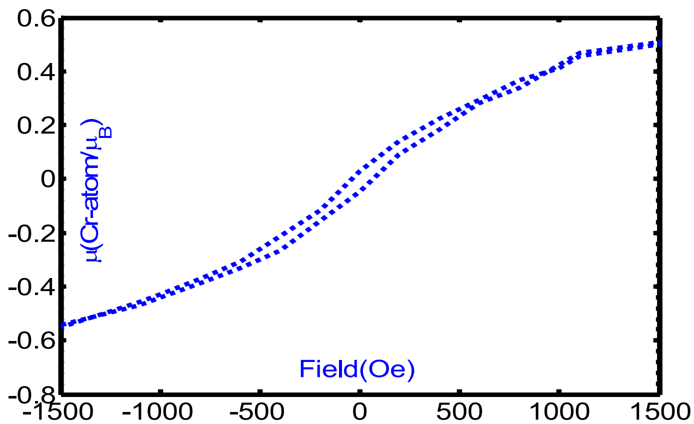

Fig. 1. Magnetization measurements indicating that the doping of Cr atoms to the In_2O_3 film and after post annealing yields a saturated magnetic moment of (0.6-0.8) μ_B per Cr atom at 10 K.

Next, the transmittance of the films were measured at normal incidence using a Bruker Optics Vertex 80 interferometer incorporating a broadband THz lamp and a room temperature KBr/DTGS-D301 photodetector. This system enabled us to perform transmittance measurements of the films over the spectral range up to 40 μm. The reflectance has been measured within broad range of angle of incidence, θ , (5,10,15,20,40,50,70,80 degrees) by the AutoSeagull reflection unit.

Fig. 2(a) demonstrates, for a ferromagnetic sample, the examples of measured frequency-dependent FTIR both the reflectance coefficient R for $\theta = 5^0$, (a) $\theta = 50^0$ (b), and the transmittance coefficient. One can see, from Fig.2, the strongly pronounced *maximum* on R curves at λ_{max}~27.8 μm, and the *minimum* on the T curve at the same frequency. We assume that these extremes correspond to the limiting spin wave frequency, ω ~ 10.8 THz, on the boundary of the Brillouin zone. Indeed, this frequency is very close to the theoretical predictions [26]. Hence, the maximum at ~ 27.8 μm is a viable candidate for the desirable effect, and we extracted the refractive index within narrow range which includes this wavelength (see below).

It would be instructive to compare reflectance spectra of ferromagnetic and non-magnetic films, with the same Cr doping parameter x, but with different oxygen deficiency, δ. Fig. 3 demonstrates the typical FTIR R spectrum for the *non-magnetic* film, with the same doping x ~0.036 as the ferromagnetic film (δ ~ 0.0087) utilized in Fig. 2, but with the oxygen deficiency, δ ~ 0.06, outside of the required range ($1.6\times10^{-4} \le \delta \le 10^{-2}$) which is required for the ferromagnetic indirect spin-spin coupling [28]. One can see, in contrast

to ferromagnetic film, that the non-magnetic film possesses *no maximum* in region 27-28 µm. Such behavior is expected, since the spin waves (magnons) which are responsible for the maximum are not presented in this specific film0. Moreover, the non-magnetic R spectrum, at 27.8 µm, shows a *minimum* instead of a *maximum*, and R is much *smaller* than R for the ferromagnetic film. One can conclude that the strongly pronounced peaks on R curve, with simultaneous extremely high reflectance R > 0.8, are the signatures of the magnon-plasmon resonance in magnetic semiconductors.

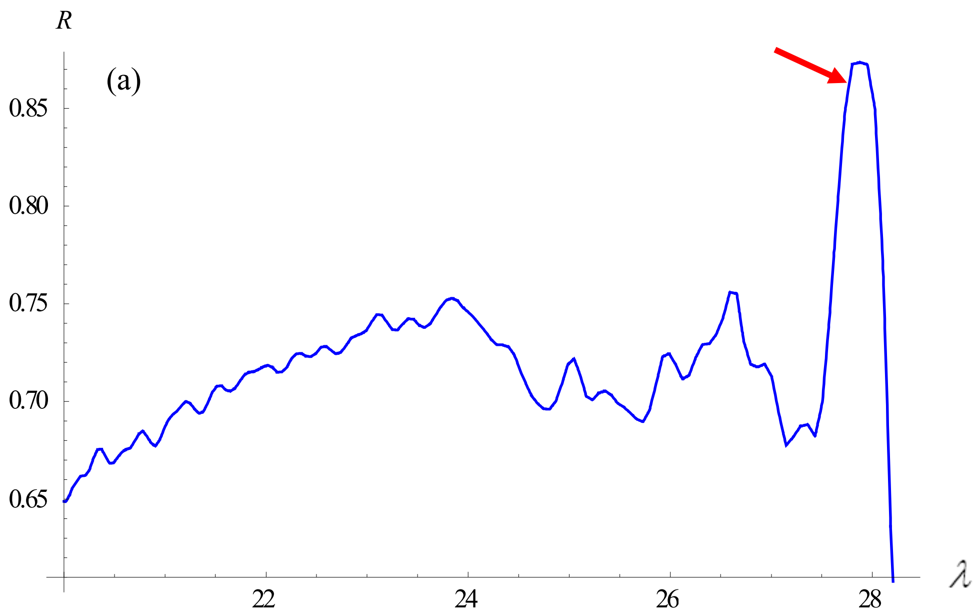

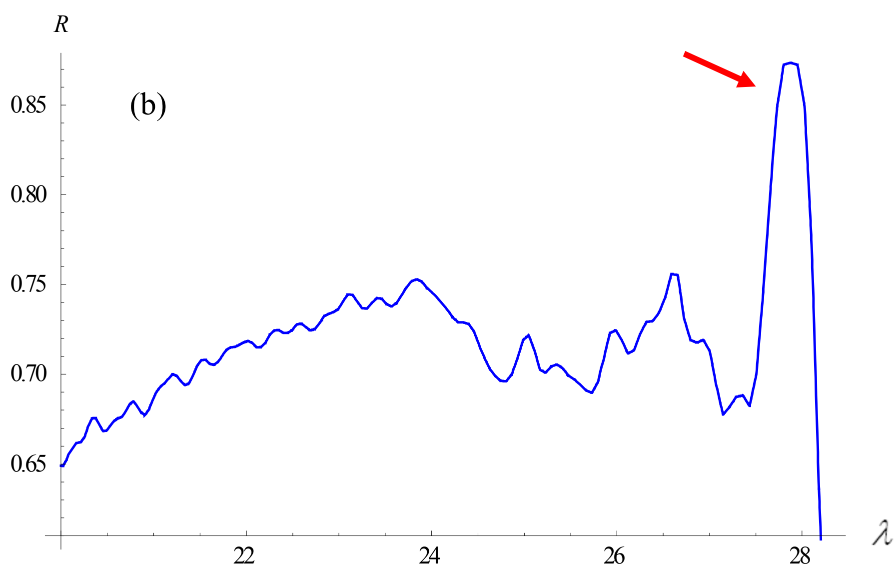

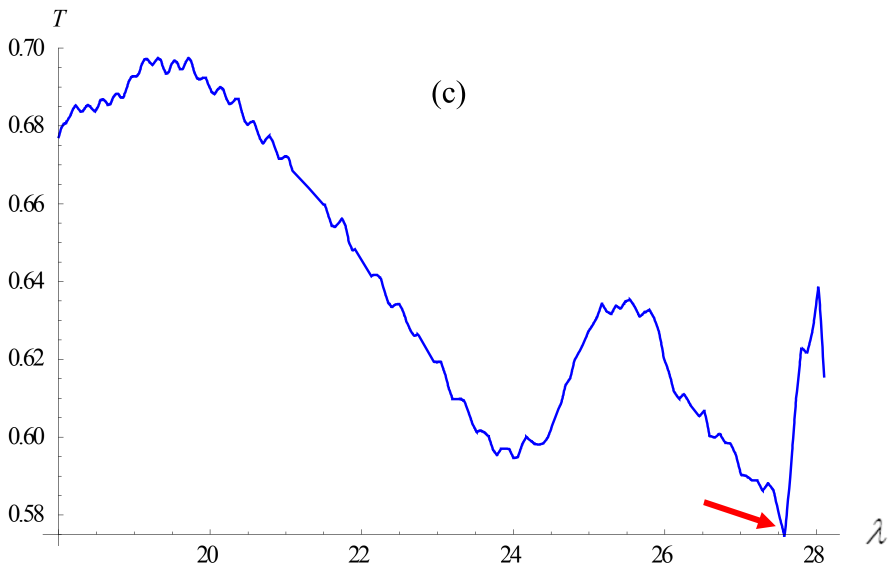

Fig. 2. Reflectance coefficient, R, and transmittance coefficient, T, of the *ferromagnetic* thin film of $In_{2-x}Cr_x O_{3-\delta}$, x~0.036, $\delta \cong 0.0087$, for different angles of incidence: a) R, θ=5°, b) R, θ=50°, c) T, θ=0°,. Red arrow points to magnon-plasmon overlapping resonance at ~ 27.8 μm, which corresponds to a maxima of R and a minima of T.

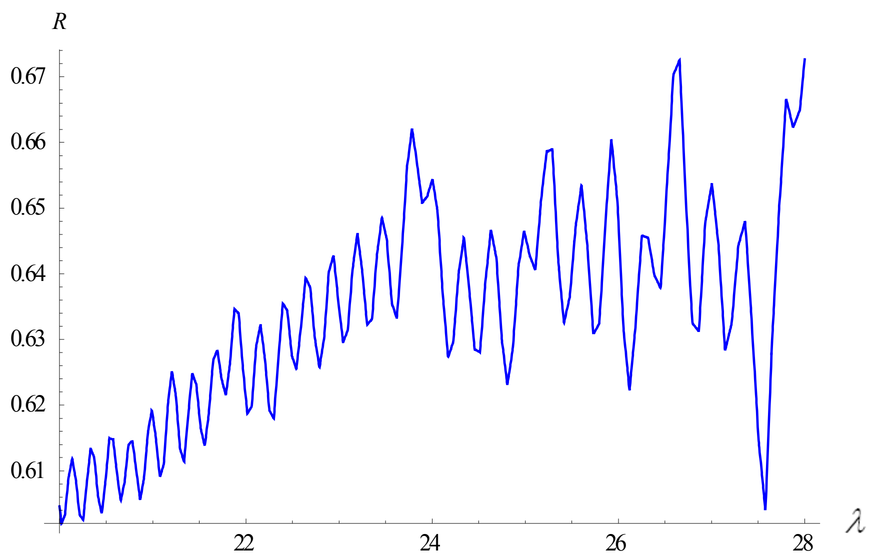

Fig. 3. Reflectance coefficient, R, of the *nonmagnetic* thin films of $In_{2-x}Cr_x O_{3-\delta}$, x~0.036, δ~ 0.06, for angle of incidence θ=50°.

2.4 Extraction Methodology

Even though FTIR measurements do not provide the *phase* of reflected and transmitted waves, the optical constants, or real and imaginary parts, $n_1(\lambda)$ and $n_2(\lambda)$, of a complex refractive index, $n(\lambda) = n_1(\lambda) + in_2(\lambda)$, can still be reliably extracted from the combined reflection and transmission amplitudes, $R(\lambda,\theta)$ and $T(\lambda,\theta)$, measured at sequence of incident angles $\theta_1,\theta_2,...\theta_l$, if this sequence covers a wide range of angles [36]. The method of the extraction of $n(\lambda)$ which was used for this project, is based on the following formulations. Obviously, each theoretically calculated curve with fixed θ for reflection and transmission $R_{TH}(\theta,n_1(\lambda),n_2(\lambda))$, $T_{TH}(\theta,n_1(\lambda),n_2(\lambda))$, should depend on $n_1(\lambda)$ and $n_2(\lambda)$. Hence, within a narrow region, close to the specific wavelength of an interest, $\lambda \sim \lambda_{ext}$, it is possible to fit calculated amplitudes $R_{TH}(\theta,n_1(\lambda),n_2(\lambda))$, $T_{TH}(\theta,n_1(\lambda),n_2(\lambda))$ to experimental data, $R(\lambda,\theta)$ and $T(\lambda,\theta)$, in order to extract the couples of optical constants $\{n_1(\theta_i,\lambda), n_2(\theta_i,\lambda)\}$ which depend on the incident angle $\theta = \theta_i$. Afterwards, one can analyze which couple $\{n_1, n_2\}$ is the same for *all* R-T amplitudes, or for the whole set $\theta = \theta_i$, and this solution should correspond to true refractive index, $n_1(\lambda_{ext}), n_2(\lambda_{ext})$.

In the calculation of the reflection–transmission amplitudes, $R_{TH}(\theta, n_1(\lambda), n_2(\lambda))$ and $T_{TH}(\theta, n_1(\lambda), n_2(\lambda))$, we have followed the classical Born's method [36] of characteristic reflection-transmission matrix of a stratified medium. This medium is the film which covers the silicon carbide substrate with thickness ~ 250 μm and permittivity $\varepsilon_S \sim 3.38 + i0.0034$ (both extrapolated from data of Ref. 37 and directly measured at wavelength ~28 μm).

The appropriate extracted refractive index band in vicinity of the magnon-plasmon resonance, at $\lambda_{max} \sim 27.8$ μm, is shown in Fig. 4. One can see, from Fig. 4, that refractive index becomes negative within narrow band with Re(n) ~ -2.0, $\mathrm{Im}(n) \approx 2.0$, which corresponds to figure of merit, *FOM* ~ 1. Hence, due to negative refractive index effect at ~ 27.8 μm, we can conclude that this wavelength consistently corresponds to assumed plasmon-magnon resonance.

As follows from Fig.4, the positive refractive index, Re(n) ~ 1.0 and Im(n) ~ 10.0, outside of the negative refractive index band. The magnitude of this refractive index can be explained from the Drude plasmon permittivity ε [22],

$$\varepsilon(\omega) = \varepsilon_\infty\left(1 - \frac{\omega_D^2}{(\omega^2 + i\gamma\omega)}\right) \qquad (1),$$

where the Drude frequency, $\omega_D \sim 310.5$ THz, corresponds to concentration of electrons ($N \sim 2.7 \times 10^{20} (1/\mathrm{cm}^3)$) in the conduction band for experimental oxygen deficiency $\delta \sim 0.0087$; $\varepsilon_\infty \sim 0.8$, and γ is the losses in plasmonic subsystem. Due to the lack of magnetic response ($\mu \sim 1$) outside the narrow band, at the boundary of the Brillouin zone [25, 26],

(which coincides approximately with the negative refractive band), the refractive index, outside the band, can be approximated as $n=\sqrt{\varepsilon}$. Since the Drude frequency is much larger than the frequency where the negative refractive index band is located ($\omega_D >> \omega_{TH}$), the calculated real part of the Drude permittivity is negative: Re(ε) ~ -100.0. The appropriate real and imaginary parts of the index of refraction are as follows: Re(n) ~ 1.0 and Im(n) ~ 10.0. Hence, as one can see from Fig. 4, real and imaginary parts of refractive index, as predicted by Drude theory, are on the same order of magnitude with experimental refractive index in the vicinity of the negative refractive index band. The behavior of $n(\lambda)$ is fully consistent both within and outside the negative refractive index band with the theoretical predictions [26, 38].

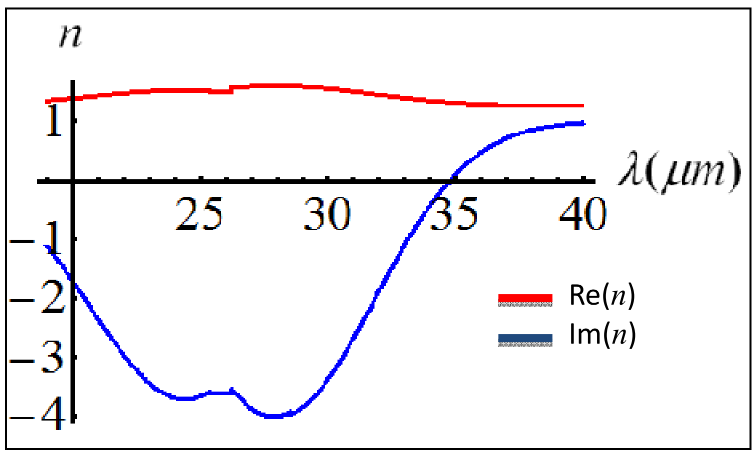

.

Fig. 4 Extracted refractive index n=Re(n)+iIm(n) in the vicinity of the plasmon-magnon resonance of the *ferromagnetic* film $In_{2-x}Cr_xO_{3-\delta}$, x~0.036, δ~ 0.0087.

In conclusion, the negative refractive index band parameters of ferromagnetic Cr-doped indium oxide thin films (i.e. wavelength and bandwidth) are fully consistent with predicted ones in Ref. 27, and the measured electric and magnetic properties of Cr-doped IO are close to those reported in literature [29]. Specifically, the experimentally verified negative refractive index narrow band, with width, $\Delta\lambda/\lambda_{max}$~0.005, is located at the limiting frequency of the magnon spectra, λ_{max}~27.8 μm, with Re(n)~ -2.0, Im(n) ~2.0. The theoretical prediction of Ref. 10 provides the negative refractive index band at λ_{max} ~ 30.0 μm with the estimated width, $\Delta\lambda/\lambda_{max}$~0.001-0.1, and the refractive index, Re(n)~ -2.5, Im(n) ~1.0. These predictions are in close proximity to the extracted experimental parameters reported above.

Conclusions

As a result of this project, we have investigated two different systems for achieving homogeneous negative index materials. Firstly, doped semiconductors exposed to special external laser beams to achieve coherent coupling of an electric dipole transition with a magnetic dipole transition leading to permeability and permittivity responses which result in negative index in a particular wavelength regime is considered. Then, magnetic semiconductors (specifically, Cr doped IO) are considered where the effect is due to the coexistence of the spin wave mode with the plasmonic mode. Both of these modes are activated by the e.m. field of the light with simultaneous permittivity and permeability responses within some frequency band, which ensures the negative refractive index within the frequency band close to the boundary of the Brillouin zone of the magnon spectra. Based on these studies presented herein, we believe that natural homogeneous magnetic semiconductors with well-pronounced negative refractive index band can be promising in future applications. The advantages of these natural materials compared with inhomogeneous composite metamaterials are their optical isotropy, and the fact that the optical constants, ε, μ, n are true physical variables defined on the atomic level, rather than some "effective" parameters.

REFERENCES

[1] M.O Oktel and O.E. Mustecaplioglu*, Phys. Rev. A* **70,** 053806 (2004).

[2] S.E. Harris, J.E. Field, and A. Imamoglu, *Phys. Rev. Lett*. **64,** 1107 (1990). \

[3] E.M. Lifshitz, L.D. Landau, and L.P. Pitaevskii, L.P." *Electrodynamics of Continuous Media*" Second Edition: (Course of Theoretical Physics, Volume 8) (Pergamon Press, London, 1984), p. 268.

[4] J. Kastel, M. Fleischhauer, S.F. Yelin, and R.L. Walsworth, *Phys. Rev. Lett*. **99,** 73602 (2007).

[5] Q. Thommen and P. Mandel, *Phys. Rev. Lett*. **96,** 53601 (2006).

[6] Jian Oi Shen, *Modern Physics Letters* **21,** vol. 21, No.12, 717 (2007).

[7] Jian Oi Shen*, Journal of Modern Optics* **53,** No. 15, 2195 (2006).

[8] B. Jungnitsch and J. Evers, Phys. Rev. A **78,** 043817 (2008)

[9] C. M. Krowne and J. Qi Shen, Phys. Rev. A **79,** 023818 (2009)

[10] C. Kittel, *Introduction to Solid State Physics*, John Wiley &Sons, New York, 1966.

[11] E.L. Nagaev, E. L., "*Physics of Magnetic Semiconductors*", (MIR Publishers, Moscow, 1983).

[12] A. Anselm, A., "*Introduction to Semiconductor Theory*", (MIR Publishers, Moscow, 1981).

[13] L.D. Landau L.D. and E.M. Lifshitz, "*Quantum Mechanics"*: (Non-Relativistic Theory, Volume 3), (Pergamon Press, 1977).

[14] M.W. McCall, A. Lakhtakia, and W.S. Weiglhofer*, Eur. J. Phys*. **23**, 353 (2002).

[15] D.R. Smith, S. Schultz, P. Markos, and C.M. Soukoulis, *Phys. Rev. B* **65,** 195104 (2002).

[16] G. B. Gonzales, J.B. Cohen, Jin-Ha Hwang, T. O. Mason, J. P. Hodges, and J. D. Jorgensen, *J. Appl*. *Phys*. **89,** 2550 (2001).

[17] I. Elfallal, R.D. Pilkington, and A.E. Hill, *Thin Solid Films* **223,** 303 (1993).

[18] J. Szczybrowski, A.Dietrich, and H. Hoffmann, *Phys. Stat. Sol*. **69,** 217 (1982).

[19] S. Zh. Karazhanov, P. Ravindran, P. Vajeeston, A. Ulyashin, T.G. Finstad, and H. Fjellvag, *Phys. Rev. B* **76,** 075129 (2007).

[20] R. Maulini, A.Moham, M. Giovanni, and J. Faist, *Appl. Phys. Lett*. **88,** 201113 (2006).

[21] R. M. Wood, "*Laser-Induced Damage of Optical Materials*", (Institute of Physics Publishing, London, 2003) p. 224.

[22] P. O. Nilsson, Applied Optics, **7**, 441 (1968).

[23] H. Mayer, Physics Duenner Schichten (Wissenschaftliche Verlagsgeschellshaft mbH., Stuttgart (1950).

[24] O. S. Heavens, *Optical Properties of Thin Solid films* (Butterworths Scientific Publications, London, 1950), pp. 136 and 139.

[25] A.G. Kussow and A. Akyurtlu, J. Nanophoton., **4**, 043514 (2010).

[26] A.G. Kussow and Alkim Akyurtlu, Phys. Rev. B, **78**, 205202 (2008).

[27] A. Pimenov, A. Loidl, P. Przyslupski, and B. Dabrowski, Phys. Rev. Lett. **95,** 247009 (2005).
[28] J. Philip, A. Punnoose, B.J. Kim, K.M. Reddy, S. Layne, J.O. Holmes, B. Satrati, P.R. Leclair, T.S. Santos and J.S. Moodera, Nature Materials **5,** 298 (2006).
[29] David J. Payne, A. Emmanuelle Marquis, Chem. Mater. **23,** 1085 (2011).
[30] L. Bizo, M. Allix M., H. Niu , M.J. Rosseinsky, Adv. Funct. Mater,. **18,** 777 (2008).
[31] K. Ueda, H. Tabata, T. Kawai, Appl. Phys. Lett. **79,** 988 (2001).
[32] Z. Jin Z, T. Fukumura, M. Kawasaki, K. Ando, H. Saito, T. Sekigushi, Y.Z.Yoo, M. Murakami., Y. Matsumoto, T. Hasegawa, H. Koinuma, Appl. Phys. Lett. **78,** 3824 (2001).
[33] Micheal A. Henderson, J. Phys. Chem. , B1999, **103**, 5328 1999.
[34] M.E. Zvanut el al., J. Appl. Phys., **104**,064122 (2008).
[35] T. Driscoll, D.N. Basov, W.J. Padilla, J.J. Mock and D.R. Smith, Phys. Rev. B **75,** 115114 (2007).
[36] M.Born and E.Wolf, *Principles of Optics* (Pergamon, Oxford, 1999).
[37] W.G. Spitzer, D. Kleinman and D.Walsh, Phys. Rev. **113**, 128 (1959).
[38] S .Zh. Karazhanov, P. Ravindran, P. Vajeeston, A. Ulyashin, T. G. Finstad, and H. Fejellvag, Phys. Rev. B **76 ,** 075129 (2007).